IEEE Access
Multidisciplinary | Rapid Review | Open Access Journal

Received 23 July 2022, accepted 29 July 2022, date of publication 4 August 2022, date of current version 10 August 2022.

Digital Object Identifier 10.1109/ACCESS.2022.3196384

RESEARCH ARTICLE

Non-Uniform Warping Sampling for Data Reduction in Planar Array Diagnostics

MARIA ANTONIA MAISTO[1,2], (Member, IEEE), MARIO DEL PRETE[1], GIOVANNI LEONE[1,2], (Member, IEEE), ROCCO PIERRI[1,2], AND RAFFAELE SOLIMENE[1,2,3], (Senior Member, IEEE)

[1]Department of Engineering, Universitá della Campania "Luigi Vanvitelli," Aversa, 81031 Caserta, Italy
[2]Consorzio Nazionale Interuniversitario per le Telecomunicazioni, 43124 Parma, Italy
[3]Department of Electrical Engineering, Indian Institute of Technology Madras, Chennai 600036, India

Corresponding author: Maria Antonia Maisto (mariaantonia.maisto@unicampania.it)

ABSTRACT The problem of detecting defective turned-off elements in antenna arrays from near-field measurements is addressed. In particular, the focus here is to reduce the number of measurements in order to positively affect the acquisition time. Such an issue is achieved by adopting the recently developed warping sampling method. Two commonly antenna diagnostics methods, i.e, the Back Transformation Method (BTM) and the Matrix Method (MM), are considered in view of this new sampling strategy and compared to the usual half-wavelength sampling. In particular, in order to identify the fault locations, outcomes returned by BTM and MM undergo a detection step based on a cell-averaging CFAR (CA)-CFAR technique borrowed from the radar literature. It is shown that the warping sampling method provides performance close to the uniform half-wavelength one with a reduced number of data. Numerical simulations are carried out in order to verify the results with different fault layouts and tapered currents.

INDEX TERMS Antenna measurements, sampling methods, array diagnostics, inverse imaging, non-uniform sampling.

I. INTRODUCTION

Array antennas are widely used in many applications such as radar, automotive, wireless communication etc. They consist of a number of radiating elements which, depending on the applications, can sometimes be very large.

An essential step in array development is the diagnostic stage, which aims at checking if the array complies with the design specifications. This entails, for example, looking for defective (faulty) elements, which from a mathematical point of view consists in solving an inverse source problem, i.e., estimating the excitation coefficients from field measurements [1]–[7].

For planar arrays diagnostics, the most commonly used method is by far the Back Transformation Method (BTM) [8]. The Matrix Method (MM) [9] is also used often as it has greater flexibility and allows to deal with generally shaped array and measurement apertures.

The associate editor coordinating the review of this manuscript and approving it for publication was Qi Luo.

Classically, measurements are collected over an aperture larger than the array support (to control truncation error [10]) over a uniform $\lambda/2$ grid. This naturally matches the standard FFT routines used to implement the BTM. However, this can yield a lot of data resulting in prolonged measurement collection time, which can be a serious inconvenience. Hence, reducing the required data would speed up the diagnostics stage.

To this end, approaches based on compressed sensing (CS) [11]–[15] have been recently explored. Indeed, by formulating the problem as the search for defective elements and by furthermore assuming that their number is low, CS allows to retrieve a sparse solution by using a number of data below the Nyquist rate [16], [17] by running a l_1 minimization. In this framework, ensuring the RIP condition is crucial. Sensing matrices, which statistically verify the RIP condition, can be built by using random matrix theory. This can be done, for example, by randomly selecting a subset of sampling positions. This method is known as random sampling (RS). However, the limitation of such an approach is that the RIP

of the sensing matrix is assured in probability. Without a proper rule to select the elements of the available ensemble, there exists a probability, even if small, that the inversion might be unstable, causing erroneous fault detection. In [15], a method to pick up a specific instance from the ensemble of possible sampling positions assuring the RIP property is proposed. However, it allows to obtain a deterministic sampling (DS) strategy for far-field measurement. Results referring to near-field measurements are not available. Also, to properly set the number of data, CS relies on the knowledge of the unknown sparsity.

The number of degrees of freedom of the radiated field (NDF) [18], [19], depending on the size of the source and the measurement aperture, can be much lower than the number of points returned by the $\lambda/2$ sampling [20]. This fact has been indeed exploited in [21], where the so-called warping method was introduced and used to derive a new deterministic near-field sampling strategy. This allowed for a remarkable reduction of data points by keeping accuracy close to the $\lambda/2$ sampling while estimating the radiation pattern [22]. This result can be in principle useful for CS as well, since the points it returns actually represent the baseline from which further data reduction can be achieved if unknown sparsity information is available. On the other hand, it allows for directly exploiting MM or BTM. Indeed, since the data points result non-uniformly arranged, BTM requires a preliminary interpolation stage. Accordingly, despite a great data reduction (as compared to the $\lambda/2$ sampling) standard inversion methods can be employed to achieve diagnostics. This is interesting since we do not need to care about RIP or to run some optimization to achieve inversion. Also, noise propagation can be better controlled because of the involved standard inversion procedures. Finally, no a priori information about the unknown sparsity (equivalent to knowing the fault percentage) is required.

Accordingly, in this contribution, we employ BTM and MM for achieving array diagnostics, by considering as faulty elements the ones that are turned off. BTM and MM return the elements that actually populate the array (i.e., the ones that are working properly), hence the defective ones can be identified as the nulls (actually minima) of the reconstructions. This can be difficult to achieve because of the noise and the filtering introduced by the inversion procedures. To cope with this limitation, faulty elements are emphasized by subtracting from the reconstructed coefficients the actual ones (assumed known) projected on the same subspace the reconstructions belong to. Also, a fault detection step follows. It consists in introducing an adaptive detection threshold determined according to the CFAR technique borrowed from radar literature [23].

Summarizing, this contribution is based on two main ingredients: the warping sampling strategy developed in [22], which allows to perform diagnostics by a significant reduction of data points as compared to the $\lambda/2$ sampling, and the application of a detection strategy to highlight the turned-off elements in the array.

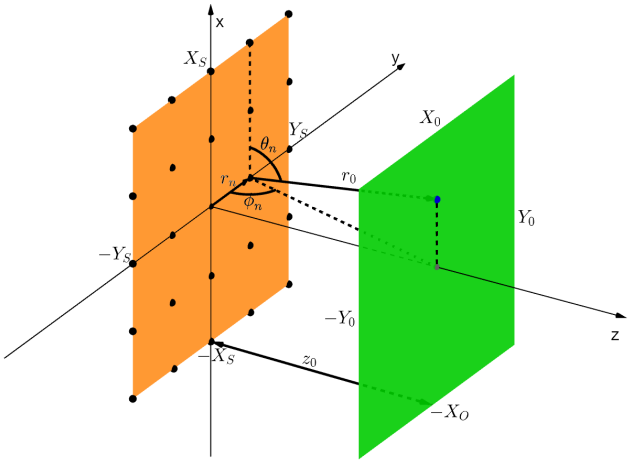

FIGURE 1. Geometry of the problem.

An extensive numerical analysis is included in order to assess the achievable performance.

II. ARRAY DIAGNOSTICS FORMULATION

Consider the antenna under test (AUT) sketched in Fig. 1. A planar array of $N = N_x \times N_y$ elements is deployed over the finite planar domain $SD = [-X_s, X_s] \times [-Y_s, Y_s]$ of the $x - y$ plane, according to a uniform rectangular grid. Denote as $\mathbf{r}_n = (x_n, y_n, 0)$ and c_n the element positions and their excitation coefficients respectively and as $\mathbf{f}$ the element factor.

The field radiated by such an antenna is collected over a planar observation domain $\mathbf{r}_0 \in OD = [-X_0, X_0] \times [-Y_0, Y_0]$ located at $z = z_0 > \lambda$, with λ being the wavelength, so that only propagating waves are relevant.

This radiation problem can be described by the following semi-discrete radiation operator

$$\mathcal{G} : \underline{c} \in C^N \rightarrow \mathbf{E}(\mathbf{r_0}) = \sum_{n=1}^{N} \mathbf{G}(\mathbf{r}_0, \mathbf{r}_n) \cdot c_n \in L^2(OD) \quad (1)$$

with

$$\mathbf{G}(\mathbf{r}_0, \mathbf{r}_n) = \frac{e^{-jkR(\mathbf{r}_0, \mathbf{r}_n)}}{4\pi R(\mathbf{r}_0, \mathbf{r}_n)} \mathbf{f}(\theta(\mathbf{r}_0, \mathbf{r}_n), \phi(\mathbf{r}_0, \mathbf{r}_n)) \quad (2)$$

$R(\mathbf{r}_0, \mathbf{r}_n) = |\mathbf{r_0} - \mathbf{r}_n|$, $\theta(\mathbf{r}_0, \mathbf{r}_n)$ and $\phi(\mathbf{r}_0, \mathbf{r}_n)$ the relative polar angles between the measurement point $\mathbf{r}_0$ and the n-th element position $\mathbf{r}_n$, and k is the wavenumber.

Measurements are collected by a probe antenna, whose plane-wave spectrum is generally flat enough to be ignored. Otherwise, a probe compensation procedure can be applied. Here, we straightway assume the ideal probe with a Dirac pulse response. Moreover, the probe is assumed linearly polarized and collecting only tangent field components $\mathbf{E_t}(\mathbf{r_0}) = \mathbf{E}(\mathbf{r_0}) \cdot \hat{t}$, with $\hat{t} = \hat{x}$ or $\hat{t} = \hat{y}$.

The array diagnostics problem aims to reconstruct the excitation coefficient vector $\underline{c}$ from field measurements. The back transformation method and the matrix method are two commonly used approaches to pursue such an objective and are briefly described below.

A. BACK TRANSFORMATION METHOD

The back transformation method is a diagnostic technique based on field plane-wave spectrum (PSW) expansion.

Say $\hat{\mathbf{E}}_t(k_x, k_y, z_0)$ the field PSW at the measurement aperture $z = z_0$, with k_x and k_y being the spatial spectral variables. Then,

$$\mathbf{E}_t(x_o, y_o, z_0) = \frac{1}{(2\pi)^2}\int_{\infty}^{\infty}\int_{\infty}^{\infty}\hat{\mathbf{E}}_t(k_x, k_y, z_0)e^{-j(k_x x+k_y y)}dk_x dk_y \quad (3)$$

with $k_z = \sqrt{k^2 - k_x^2 - k_y^2}$. Now, since

$$\hat{\mathbf{E}}_t(k_x, k_y, z_0) = \hat{\mathbf{E}}_t(k_x, k_y, 0)e^{-jk_z z_0} \quad (4)$$

after compensating the propagation term and the element factor, an estimate of the excitation coefficients c_n is obtained as

$$\hat{c}_n = \int_{-\infty}^{\infty}\int_{-\infty}^{\infty}\frac{k_z e^{jk_z z_0}}{\mathbf{f}_t(k_x, k_y)}\hat{\mathbf{E}}_t(k_x, k_y, z_o)e^{-j(k_x x_n+k_y y_n)}dk_x dk_y \quad (5)$$

with $\mathbf{f}_t = \mathbf{f}\cdot\hat{t}$ being the tangent component of the element factor. It is seen that estimating the excitation coefficients via BTM entails computing a couple of Fourier transformations, one for field PWS evaluation and one for achieving back-propagation. This can be achieved by employing an FFT routine, which makes the method appealing because of its quick implementation. Usually, the field is sampled at $\lambda/2$, λ being the wavelength, which is equivalent to restricting the band to the so-called visible domain, i.e., evanescent contribution is filtered out. Note that restricting the spatial spectrum implicitly regularizes the inverse problem of retrieving c_n from field measurements $\mathbf{E}_t(k_x, k_y, z_0)$, which is indeed ill-posed. This is easily seen by looking at the exponential term $e^{jk_z z_0}$, which diverges for $k_x^2 + k_y^2 > k^2$. However, (5) does not return the least square solution because of the finite size of the measurement aperture. This of course negatively affects the performance achievable in the reconstructions (truncation error) [10].

B. MATRIX METHOD (MM)

Since field data are collected over a finite discrete set of points belonging to OD, instead of the operator in (2), what one should actually consider is the matrix operator

$$\mathbf{A} : \underline{c} \in C^N \rightarrow \underline{E}_t = \mathbf{A}\cdot\underline{c} \in C^M \quad (6)$$

where $\underline{E}_t$ is the numerical vector consisting of the samples of $\mathbf{E}_t$ collected over the M measurement points $\mathbf{r}_{0m}$ and $\mathbf{A}$ is a matrix whose entries are given by

$$A_{mn} = \frac{e^{-jkR_{mn}}}{4\pi R_{mn}}\mathbf{f}_{tmn} \quad (7)$$

where $R_{mn} = |\mathbf{r}_{0m} - \mathbf{r}_n|$ and $\mathbf{f}_{tmn}$ is the tangent component of the element factor linking the element at $\mathbf{r}_n$ to the observation point at $\mathbf{r}_{0m}$. The MM, hence, entails recovering the excitation vector $\underline{c}$ by solving the matrix equation (6), typically in the least square sense since $M > N$ and because of noise and uncertainty. Clearly, MM is more computationally demanding than BTM, with the actual computational cost being related to the employed solution algorithm. Indeed, direct or iterative inversion schemes can be exploited. However, MM is more flexible since it allows to just as easily deal with measurement aperture and array antenna of general shapes (i.e., not necessarily planar). Data collected over a non-uniform grid can be addressed as well.

Regardless of the inversion method one may want to use, said $\{\sigma_n, \underline{u}_n, \underline{v}_n\}_{n=0}^N$ the singular system of $\mathbf{A}$, the retrieved excitation vector can be formally written as

$$\hat{\underline{c}} = \sum_{n=0}^{N} W_n \frac{< \underline{E}_t + \underline{N}, \underline{v}_n >}{\sigma_n}\underline{u}_n \quad (8)$$

where $< \cdot, \cdot >$ denotes the scalar product, $\underline{N}$ is the noise vector that corrupts data and W_n is a filtering window that depends on the adopted inversion scheme and regularizes the problem. Regularization depends on the noise level and, of course, impacts on the achievable performance. However, in general, MM can allow a for better performance than BTM, since the latter "imposes" regularization regardless of the noise level.

Related to the previous question there is the strategy adopted to design the measurement set-up in terms of the number and the location of the measurement points. This crucial aspect is where we mainly contribute in this paper as detailed in the next section.

III. FIELD SAMPLING

As mentioned above, retrieving the excitation coefficients entails solving a finite dimensional ill-posed linear inverse problem, which basically inherits ill-posedness from the related continuous inverse source problem of which it is the discrete counterpart. More in detail, it has been shown that the "continuous" radiation operator (i.e., operator in (1) acting on $L^2(SD)$) presents a distinctive singular value behaviour. Indeed, the singular values are rather constant till a critical index beyond which they experience an exponentially fast decay. This critical number is the so-called number of degrees of freedom (NDF) of the problem and basically means that the dimension of the radiated field space (i.e., the data space) is essentially of finite dimension. Accordingly, the number of spatial measurements, and their positions, should be dictated by the NDF (indeed slightly greater) so as to approximate such a finite dimensional space.

By the usual uniform $\lambda/2$ sampling, $M > N >$ NDF. This is because in order to reduce truncation error the measurement aperture is commonly set larger than the array size. Also, note that typically NDF $< N$, that is lower than the number of elemental radiators uniformly deployed at a $\lambda/2$ step over the array planar aperture. It has been shown that the NDF $\rightarrow N$ only when the measurement aperture becomes unbounded, which is obviously unfeasible. More in detail, the

NDF was analytically estimated in [20] as

$$\mathrm{NDF} = \frac{4}{\lambda^2}\left[\sqrt{(X_0+X_S)^2+z_0^2}-\sqrt{(X_0-X_S)^2+z_0^2}\right] \times\left[\sqrt{(Y_0+Y_S)^2+z_0^2}-\sqrt{(Y_0-Y_S)^2+z_0^2}\right] \quad (9)$$

with $[\cdot]$ being the operator that retains the least greatest integer. From (9) it is easily seen that when $X_0, Y_0 \to \infty$ then $\mathrm{NDF} \to 16X_SY_S$, which is exactly N, that is the number of radiators populating the array. Therefore, when $M > N > \mathrm{NDF}$, the singular values of the discrete operator (6) run beyond the NDF and hence very low singular values may lead to instability in the reconstruction (ill-posedness) [24]. This is circumvented in the BTM, since it implicitly regularizes the problem, whereas in the MM one has to properly choose the regularizing sequence W_n.

Since the radiated field space has essentially dimension NDF, it is natural to try to exploit only a number of measurements of the same order as the NDF. However, the measurement points should be set so that the singular values of the discrete operator $\mathbf{A}$ approximate the ones of $\mathcal{G}$ in the region preceding the abrupt decay. If this is possible, a great data reduction is achieved with consequent data collection time saving, especially for large or very large (in terms of wavelength) array antennas.

This crucial point has been recently successfully pursued in [21], [22]. There, a field sampling strategy, that requires a number of measurements M only slightly greater than the NDF reported in (9), was derived. This approach is based on a proper reformulation of the radiation operator that highlights the radiated field as a spatially varying bandlimited function, that is, as a function whose bandwidth depends on the observation point $\mathbf{r_0}$. More in detail, it is shown that upon introducing suitable transformations that ''warp'' the original observation variable $\mathbf{r}_0$, the radiated field can be expressed as a classical band-limited function and thus the Shannon sampling theorem can be employed. The transformations are shown in eq. (10), whereas the theoretical details are reported in [22].

$$\xi_x = \alpha_x(x_0)\frac{k}{2}\left(\sqrt{(x_0+X_S)^2+z_0^2}-\sqrt{(x_0-X_S)^2+z_0^2}\right)$$
$$\xi_y = \alpha_y(y_0)\frac{k}{2}\left(\sqrt{(y_0+Y_S)^2+z_0^2}-\sqrt{(y_0-Y_S)^2+z_0^2}\right) \quad (10)$$

where α_x and α_y are given by

$$\alpha_x(x_0) = 1-(1-\nu)\sin^4\left(\frac{\pi}{2X_0}x_0\right)$$
$$\alpha_y(y_0) = 1-(1-\nu)\sin^4\left(\frac{\pi}{2Y_0}y_0\right) \quad (11)$$

Indeed, ν is an oversampling factor so that $M = \nu^2\mathrm{NDF}$ and the sin terms allow to achieve a spatially varying oversampling so as to deploy more points where required (see [22]). Accordingly, the following sampling series can be exploited

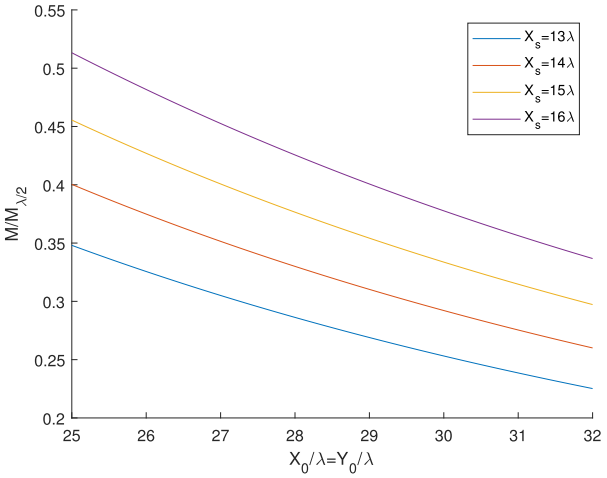

FIGURE 2. The ratio between M and $M_{\lambda/2}$ as function of $X_0 = Y_0$ for different values of X_S.

to represent the field

$$\mathbf{E}_t(\xi_x,\xi_y) = e^{j\gamma_x(\xi_x)}e^{j\gamma_y(\xi_y)}\sum_{s=1}^{N_x}\sum_{l=1}^{N_y}\mathbf{E}_t(\xi_{xs},\xi_{yl}) \times e^{-j\gamma_x(\xi_{xs})}e^{-j\gamma_y(\xi_{yl})}\mathrm{sinc}(\xi_x-\xi_{xs})\mathrm{sinc}(\xi_y-\xi_{yl}) \quad (12)$$

with

$$\gamma_x(x_0) = \frac{k}{2}\left[\sqrt{(x_0+X_S)^2+z_0^2}+\sqrt{(x_0-X_S)^2+z_0^2}\right]$$
$$\gamma_y(y_0) = \frac{k}{2}\left[\sqrt{(y_0+Y_S)^2+z_0^2}+\sqrt{(y_0-Y_S)^2+z_0^2}\right] \quad (13)$$

Finally, the sampling points are evaluated by solving

$$\xi_x(x_{0s}) = \xi_{xs} = s\pi$$
$$\xi_y(x_{0l}) = \xi_{yl} = l\pi \quad (14)$$

with s, l being integer numbers. It is seen that, since (ξ_x, ξ_y) are non-linearly linked to (x_0, y_0), uniform sampling in (ξ_x, ξ_y) becomes non-uniform in $\mathbf{r}_0$. This could be expected in view of the spatially varying behaviour of the radiation operator in the near-field. Nonetheless, as remarked above, a considerable reduction of data points is achieved.

Fig. 2 shows the ratio between the number of measurements $M = \nu^2\mathrm{NDF}$ returned by non-uniform sampling and $M_{\lambda/2}$, the number of measurements point corresponding to the uniform $\lambda/2$ sampling, as function of the observation domain size $X_0 = Y_0$ for different values of $X_S = Y_S$ and by choosing $\nu = 1.2$. As can be seen, such a ratio is always lesser than 1. Hence, the proposed sampling strategy allows to decrease the measurement number compared to the classical $\lambda/2$ sampling. In particular, the data reduction (with respect to $M_{\lambda/2}$) becomes dramatic as the array size (and consequently the measurement aperture) increases.

Clearly reducing the number of measurement points is positive since data acquisition time is reduced as well. Also, MM enjoys a lighter computational burden since it is required

to deal with a smaller matrix. BTM, instead cannot be employed directly. However, the series in (12) allows to interpolate the field over a $\lambda/2$ grid and then BTM can still employed.

The crucial question is to see how data reduction, allowed by the non-uniform sampling, affects performance in the reconstructions, compared to the $\lambda/2$ sampling. To this end, in the next section some examples of array diagnostics are provided.

IV. NUMERICAL EXAMPLES

We consider an array of $N = 2809$ dipoles directed along the x axis, uniformly spaced at $\lambda/2$ and arranged over the array support $X_s = Y_s = 13\lambda$. The x component of the radiated field is collected over a planar observation domain with $X_0 = Y_0 = 25\lambda$ and $z_0 = 8\lambda$. The field is generated by the Phased-array toolbox of MATLAB. In particular, since such a toolbox accepts voltage taper, the desired excitation currents have been scaled by the antenna input impedance provided by the MATLAB toolbox itself.

Two different excitation distributions are considered: uniform, with $c_n = 1 \ \forall n$, and an $\bar{n} = 4$ Taylor distribution with side-lobe level $SLL = 20dB$. For comparison purposes, data are collected by exploiting both the usual $\lambda/2$ sampling and the non-uniform one returned by eq. (14). The first sampling scheme requires $M_{\lambda/2} = 10201$, whereas the non-uniform one $M = 3600$ (i.e., only 35% of $M_{\lambda/2}$).

We focus on detecting defective elements. To this end, a fraction of the overall excitation coefficients is turned off according to a uniform probabilistic law. Both the MM and BTM are employed to reconstruct the excitation coefficients and each of them is checked for both the sampling schemes under comparison. Therefore, we have actually four reconstruction schemes, with BTM proceeded by interpolation (as mentioned above) when applied to the data obtained over the non-uniform grid. Finally, data are corrupted by a zero mean complex white Gaussian noise whose signal to noise ratio (SNR) is

$$\mathrm{SNR} = \frac{||\underline{\mathrm{E}}_t||}{||\underline{\mathrm{N}}||} \tag{15}$$

Fig. (3) shows two random faulty deployments for the case of uniform and Taylor excitation coefficients. In particular, the number of faulty elements was set at $3\%N$ ($N_{fault} = 87$) and the field data corrupted by noise with $SNR = 20dB$. The corresponding reconstructed excitation coefficients are shown in Fig.4 and Fig. 5. In particular, the MM reconstructions have been obtained by employing a truncated singular value decomposition (TSVD) inversion scheme and retaining the singular values above $-20dB$ the maximum one. In both figures the top rows refer to MM and the bottom ones to BTM, instead the first columns have been obtained by considering the uniform $\lambda/2$ sampling whereas the right column using the non-uniform sampling. It can be appreciated that, from the considered singular value truncation threshold, the MM and the BTM reconstructions look very similar. What is more, this holds true for both the sampling schemes, in spite of the reduction in the number of measurements of the non-uniform sampling. This is sufficient to state that the non-uniform sampling scheme actually captures the same information as the $\lambda/2$ sampling. Also, it can be noted that most of the faulty elements are already clearly detectable, especially for the uniform excitation. However, for the Taylor's taper, discerning from faults and excitation coefficients becomes increasingly hard in the region where the latter are very low. This issue can be remedied by employing a suitable detection strategy.

V. FAULT DETECTION

To begin with, first the difference excitation coefficients are built. In particular, the difference coefficients are defined as $\Delta\underline{c} = \mathcal{P}\underline{c} - \hat{\underline{c}}$, where $\hat{\underline{c}}$ are the reconstructed coefficients and $\mathcal{P}\underline{c}$ are the actual excitation coefficients (assumed known) that have undergone the same filtering ($\mathcal{P}$ represents the corresponding projection operator) as due to the reconstruction procedure. For example, for the MM (similar arguments apply for BTM), it yields

$$\Delta\underline{c} = \sum_{m\in I_{fault}} \sum_{i=1}^{N_T} c_m u_i^*(m)\underline{u}_i + \sum_{i=1}^{N_T} \frac{< \underline{\mathrm{N}}, \underline{\mathrm{v}}_i >}{\sigma_i}\underline{u}_i \tag{16}$$

where N_T is the TSVD truncation index and I_{fault} is the set of positions where faults occur. It is noted that knowing $\mathcal{P}\underline{c}$ is equivalent to knowing the field radiated by the array when all elements work correctly, as commonly done in many papers concerning array diagnostics [11]–[15]. Also, eq. (16) can be expressed in terms of the point-spread function (psf) of the adopted inversion scheme as

$$\Delta\underline{c} = \sum_{m\in I_{fault}} c_m \mathrm{psf}(n,m) + \sum_{i=1}^{N_T} \frac{< \underline{\mathrm{N}}, \underline{\mathrm{v}}_i >}{\sigma_i}\underline{u}_i \tag{17}$$

which is useful for later discussion.

Detection is then achieved by turning $\Delta\underline{c}$ into a binary vector populated by 1 where $|\Delta c(n)|^2 \geq A_{th}$, A_{th} being the detection threshold, and 0 elsewhere.

The choice of the detection threshold is a crucial issue. Indeed, it must be set in order to establish a proper balance between the probability of false alarm (PFA) and the probability of detection (PD). In the case of a single fault, and under the assumed working condition, analytical results that link A_{th} and PFA and PD can be established, as done in [25]. However, when multiple faults occur, because of the linkage between the reconstructions of the different faults, those results can be expected to hold only when the faults are well separated. The point is that one does know which is the arrangement of the faults.

To cope with this issue, we propose to apply a constant false-alarm rate (CFAR) method, borrowed from radar literature [23], which sets an adaptive threshold in order to keep the false-alarm probability constant. In particular, we adopt the cell-averaging CFAR (CA)-CFAR. By this method, the detection threshold for a specific array element under test is

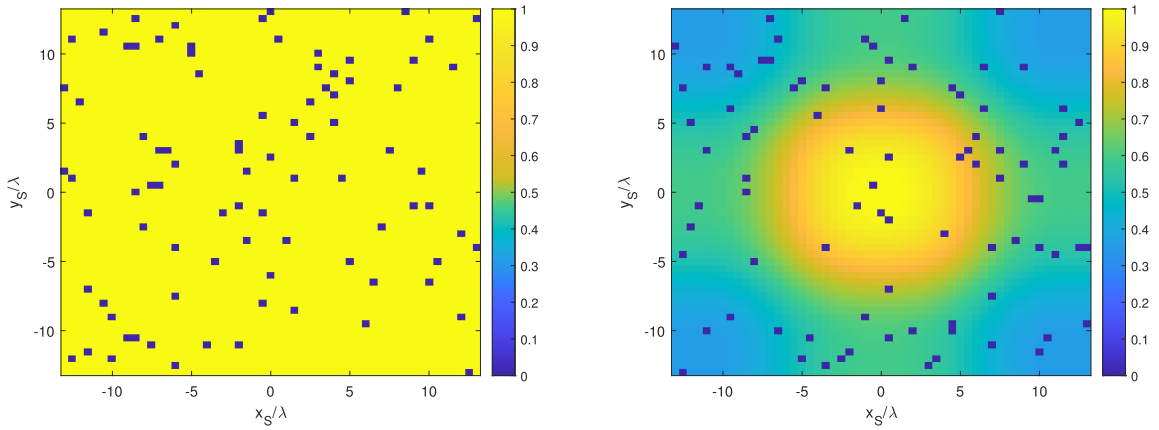

FIGURE 3. Amplitude of the excitation coefficients with faults for a planar array $SD = [-Xs, Xs] \times [-Ys, Ys]$ and $N = 2809$ dipoles arranged at $\lambda/2$. Panel (a) refers to a uniform distribution whereas panel (b) to an $\bar{n} = 4$ Taylor distribution with $SLL = 20dB$. In both cases $N_{faults} = 3\%N$ are denoted as blue squares.

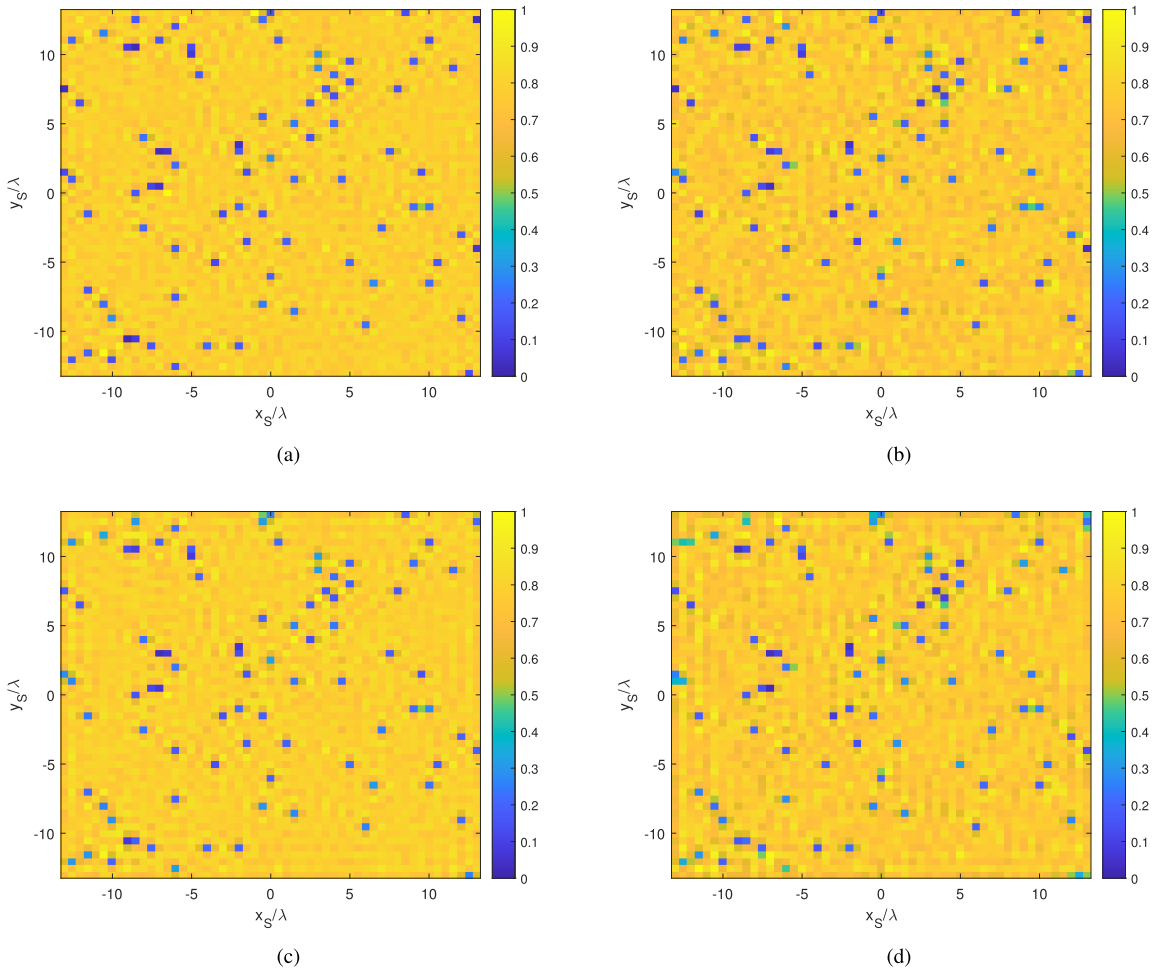

FIGURE 4. Amplitude reconstruction results for the case of uniform distribution reported in Fig. 3 panel (a). The measurement parameters are $OD = [-X_0, X_0] \times [-Y_0, Y_0]$ with $X_0 = Y_0 = 25\lambda$ and $z_0 = 8\lambda$. Panel (a), refers to MM and $M_{\lambda/2}$=10201, panel (b) to MM and M=3600, panel (c) to BTM and $M_{\lambda/2}$=10201 and panel (d) to BTM and M=3600. In this last case, the data M are first interpolated on a $\lambda/2$ grid and then the BTM is applied. Finally, $SNR = 20dB$.

determined by averaging over some neighbouring cells. More in detail, consider the vector $\Delta\underline{c}$ arranged in matrix form $\Delta\underline{C} \in C^{N_x \times N_y}$, with N_x and N_y being the number of elemental radiators along x and y, respectively, and $N = N_x N_y$. Then, the element at (t, s) corresponds to the n array element with $n = (s-1)N_x + t$, $t \in (1, 2, \cdots, N_x)$ and $s \in (1, 2, \cdots, N_y)$.

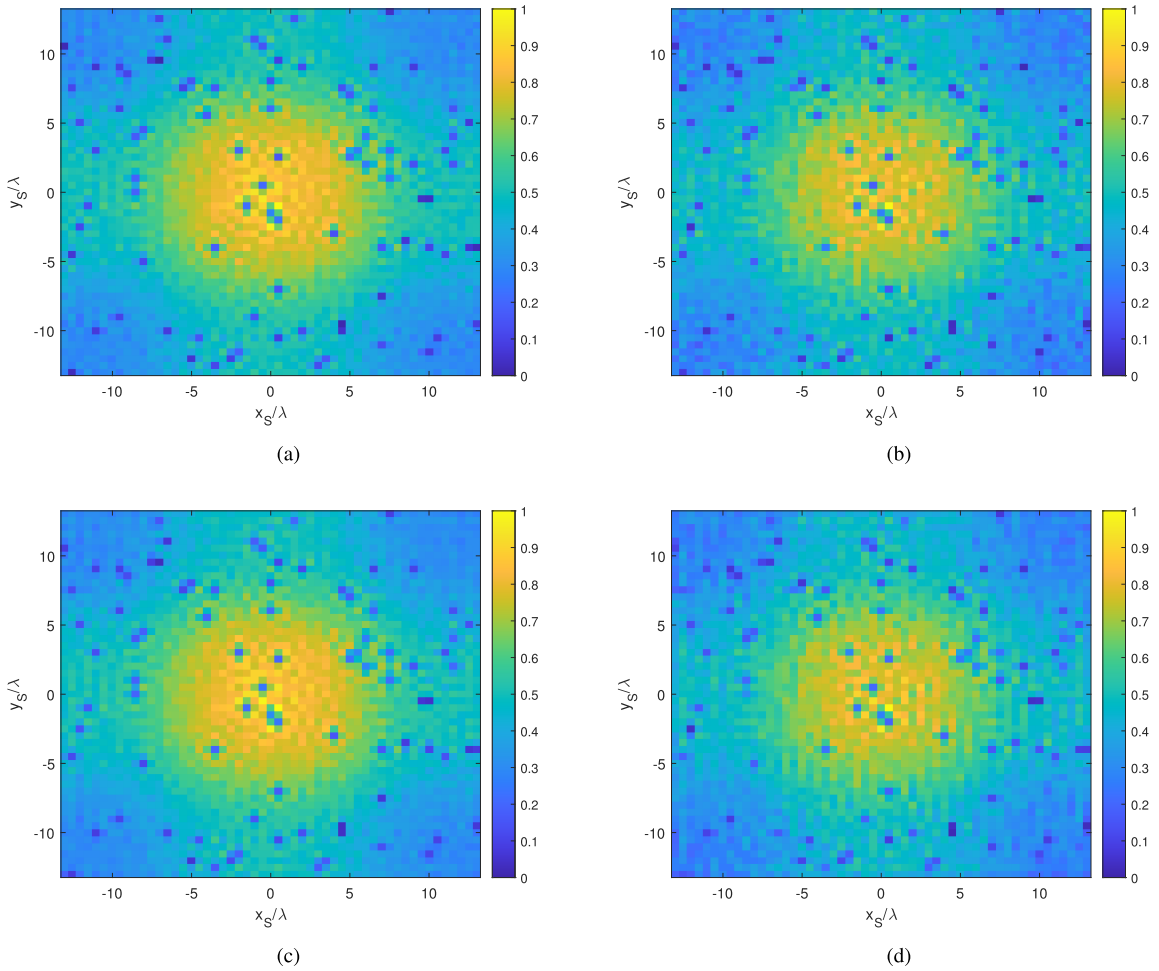

FIGURE 5. Amplitude reconstruction results for the case of Taylor distribution reported in Fig. 3 panel (b). The measurement parameters are $OD = [-X_0, X_0] \times [-Y_0, Y_0]$ with $X_0 = Y_0 = 25\lambda$ and $z_0 = 8\lambda$. Panel (a), refers to MM and $M_{\lambda/2}$=10201, panel (b) to MM and M=3600, panel (c) to BTM and $M_{\lambda/2}$=10201 and panel (d) to BTM and M=3600. In this last case, the data M are first interpolated on a $\lambda/2$ grid and then the BTM is applied. Finally, $SNR = 20dB$.

The detection threshold for the pixel (t, s) of the reconstruction is evaluated by first averaging the reconstruction over neighbour cells belonging to a rectangular window of $K = K_1 \times K_2$ elements, that is

$$Y(t,s) = \sum_{(l,p)\in I_T - I_{guard}} \frac{|\Delta C(l,p)|^2}{LP} \tag{18}$$

with I_T being the rectangle window centered in (t, s) and sides $K_1 + N_{guard1}$ and $K_2 + N_{guard2}$, and I_{guard} the rectangle window centered in (t, s) and sides N_{guard1} and N_{guard2}. $Y(t, s)$ actually represents an estimate of the background noise (interference). Eventually, the detection threshold is obtained by multiplying the estimated average by a scaling factor α_T. The latter allows to control the false alarm probability by

$$\mathrm{PFA}_d = \left(1 + \frac{\alpha_T}{K}\right)^{-K} \tag{19}$$

Hence, by setting PFA_d, α_T is evaluated from (19) and the detection threshold is finally set equal to $A_{th} = \alpha_T Y$.

Note that in (18), the element under test and its immediate neighbours belonging to I_{guard} are excluded by the averaging procedure. This is done in order to avoid biasing the estimation of the threshold towards excessively high values. In this regard, N_{guard1} and N_{guard2} must be properly chosen according to the psf function which describes how the fault reconstruct actually spreads over more than one pixel point. In [20], an analytical estimation in terms of the configuration's geometrical parameters is derived. This result can then be used to set the guard pixels as those for which the main-lobe of the psf is excluded by the averaging procedure. More in detail, it is shown that only when $X_0 \to \infty$ and $Y_0 \to \infty$, the main-lobe half-width of the psf tends to $\lambda/2$, otherwise it is larger and non-uniform across the array domain. In particular, for the cases considered in this manuscript, the psf estimate reported in [20] suggests to set $N_{guard1} = N_{guard2} = 1$.

The detection threshold resulting from (18) and (19) does not properly take into account the contributions of the reconstructions of the faults that can enter the averaging window. The result is that noise estimation is distorted and generally

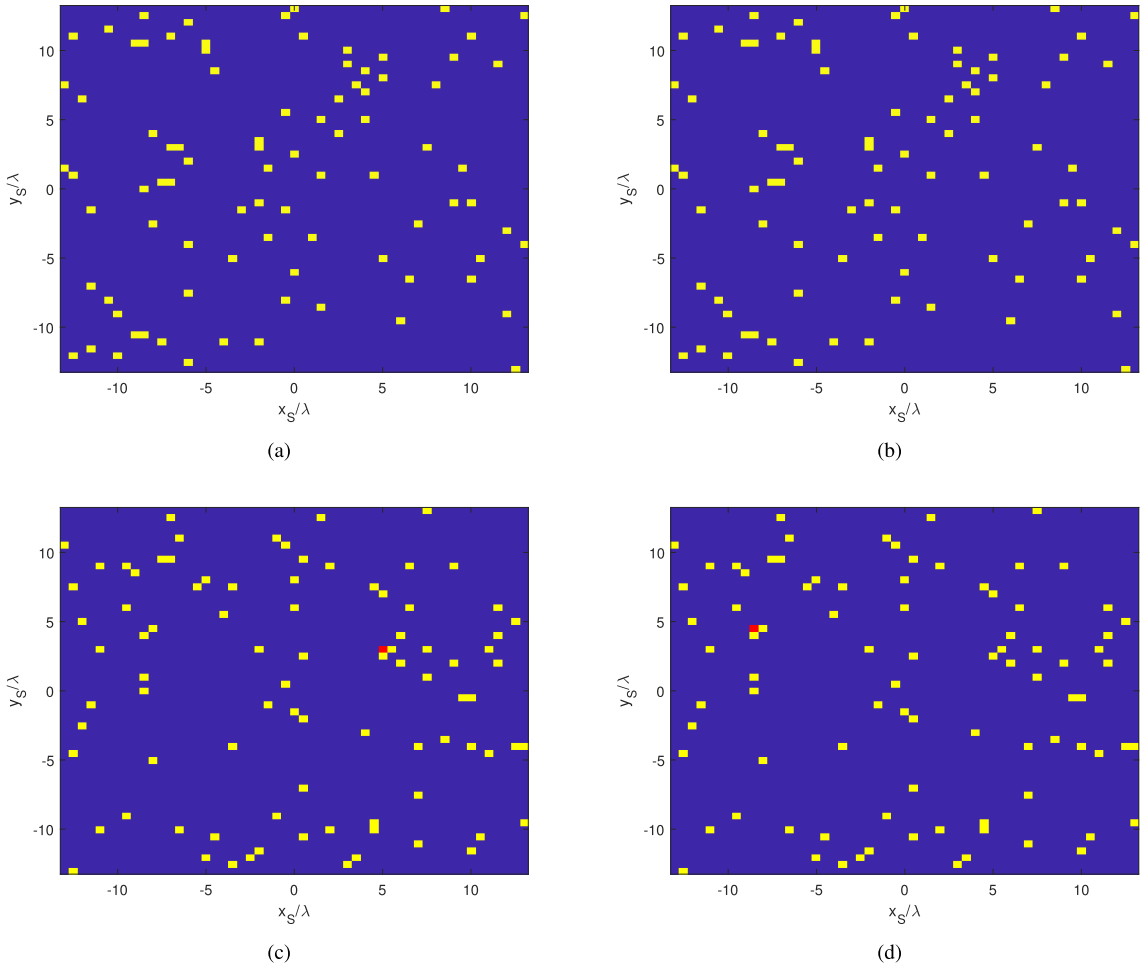

FIGURE 6. Detection with the MM method. Panels (a) and (b) refer to the uniform distribution, panels (c) and (d) to the Taylor one. In panels (a) and (c) uniform $\lambda/2$ sampling with $M_{\lambda/2} = 10201$ is employed whereas in panels (b) and (d) the non-uniform sampling one with $M = 3600$, respectively. The configuration parameters are the same as in Fig. 4, whereas $PFA_d = 10^{-3}$. Detected faults are displayed as yellow squares whereas false positives as red squares.

increases the threshold. This leads to a deviation between the set PFA_d and the actual one. Accordingly, also K_1 and K_2 must be judiciously chosen.

Indeed, K_1 and K_2 must be chosen so as to make the noise power estimation reliable across all of the array element positions. In principle, larger K_1 and K_2 imply better noise power estimation. However, this is not necessarily true when more than one fault is present. In fact, excessively large K_1 and K_2 can decrease the detection threshold reliability because other faults are included in the averaging due to the strong interference of the main lobes. After some trials, we set $K_1 = K_2 = 10$.

Now we are ready to assess the detection performance. To this end, as a preliminary example, we just address the case reported in Fig. 3. In particular, since BTM and MM return similar results, we show only the detection concerning the MM method. The outcome of the detection is reported in Fig. 6, where $SNR = 20dB$ and the detection threshold A_{th} is set by fixing $PFA_d = 0.001$. As can be seen, in both the cases, the faults are clearly and correctly detected and localized. Remarkably, this holds true also for the non-uniform sampling strategy. The case of Taylor distribution also shows many false positives (for both sampling methods).

These results show that the suggested data reduction strategy actually works. However, it is not conclusive since it refers to just one example. In order to estimate the probability of detection and of false alarm we run a Monte Carlo analysis by considering $N_{trials} = 1000$ different realizations of noise and fault layouts. In particular, PFA and PD are evaluated as

$$\text{PFA} = \frac{1}{N_{trials}} \sum_{n=1}^{N_{trials}} \frac{FP(n)}{N - N_{fault}} \tag{20}$$

and

$$\text{PD} = \frac{1}{N_{trials}} \sum_{n=1}^{N_{trials}} \frac{FD(n)}{N_{fault}} \tag{21}$$

where FP, FD and N_{fault} denote the number of false positives, the number of detected faults and the number of faults,

TABLE 1. Detection results for the case of uniform excitation coefficients. The geometrical parameters are the same as in Fig. 4.

SNR	Faults	$PD_{\lambda/2}$	PD_{nu}	$PFA_{\lambda/2}$	PFA_{nu}
15 dB	29	1	0.992	3.55×10^{-3}	1.43×10^{-3}
20 dB	29	1	1	1.20×10^{-3}	8.09×10^{-4}
25 dB	29	1	1	1.84×10^{-3}	1.47×10^{-3}
30 dB	29	1	1	2.23×10^{-3}	2.35×10^{-3}
15 dB	87	1	0.913	9.83×10^{-4}	8.49×10^{-4}
20 dB	87	1	0.997	2.33×10^{-4}	2.33×10^{-4}
25 dB	87	1	1	2.44×10^{-4}	2.88×10^{-3}
30 dB	87	1	1	2.73×10^{-4}	3.58×10^{-3}
15 dB	145	0.925	0.722	5.14×10^{-4}	4.67×10^{-4}
20 dB	145	0.989	0.944	6.27×10^{-5}	8.18×10^{-5}
25 dB	145	0.993	0.985	7.66×10^{-5}	8.63×10^{-5}
30 dB	145	0.994	0.992	7.77×10^{-5}	9.53×10^{-5}

TABLE 2. Detection results for the case of Taylor tapered excitation coefficients with $SLL = -20dB$ and $\bar{n} = 4$. The geometrical parameters are the same as in Fig. 5.

SNR	Faults	$PD_{\lambda/2}$	PD_{nu}	$PFA_{\lambda/2}$	PFA_{nu}
15 dB	29	0.997	0.850	3.25×10^{-3}	1.25×10^{-3}
20 dB	29	1	0.981	1.37×10^{-3}	8.65×10^{-4}
25 dB	29	1	1	2.03×10^{-3}	1.50×10^{-3}
30 dB	29	1	1	2.40×10^{-3}	2.32×10^{-3}
15 dB	87	0.914	0.710	8.31×10^{-4}	6.05×10^{-4}
20 dB	87	1	0.984	2.54×10^{-4}	2.37×10^{-4}
25 dB	87	0.995	0.971	2.88×10^{-4}	2.95×10^{-4}
30 dB	87	0.997	0.990	3.06×10^{-4}	3.49×10^{-4}
15 dB	145	0.734	0.547	4.16×10^{-4}	3.10×10^{-4}
20 dB	145	0.864	0.755	8.03×10^{-5}	8.60×10^{-5}
25 dB	145	0.890	0.842	8.18×10^{-5}	9.42×10^{-5}
30 dB	145	0.897	0.871	7.32×10^{-5}	9.50×10^{-5}

respectively. Different values of SNR and N_{faults} are also considered for each sampling strategy, uniform and non uniform (nu). In particular, the results concerning the uniform distribution are shown in the Table 1, whereas Table 2 refers to the Taylor distribution. In both cases, the threshold is chosen by fixing PFA_d equal to 0.001.

As can be seen, uniform sampling generally returns results which are only very slightly better than the non-uniform sampling. Actually, they are really very close, and hence demonstrate the effectiveness of the non-uniform sampling strategy. Also, as expected, PD degrades when SNR reduces and/or the number of faults increases. For the Taylor distribution, as natural, this is a bit more evident. Nonetheless, in all the cases, the results keep to satisfying values, also considering that if antenna diagnostics is performed in controlled environments like an anechoic chamber, the *SNR* can be sufficiently high. Finally, it is noted that PFA decreases when the number of faults increases. This, at first glance, could appear contour-intuitive but it is actually a consequence of the chosen detection strategy. Indeed, when many faults are present (18) tends to return higher detection thresholds and hence lower PFA. As anticipated above, this is how fault reconstructions distort threshold setting.

VI. CONCLUSION

In this paper, the problem of planar array antenna diagnostics from near-field measurements has been addressed. In particular, the standard Back transformation and the Matrix methods have been considered in view of the new field sampling strategy proposed in [22]. The latter provides a non-uniform sampling grid that allows to reduce the number of measurement points compared to the standard $\lambda/2$ strategy, resulting in a decrease of the measurement acquisition time. In particular, for MM this positive impact becomes even more relevant because the reduction in the number of points also decreases the computational burden.

Since from the reconstructions it is quite difficult to identify the fault locations, a fault detection step has been added to the array diagnostic problem. Such a step introduces an adaptive threshold related to a reference current and relies to a cell-averaging CFAR (CA)-CFAR technique [23]. It allows to choose a detection threshold which keeps the false-alarm probability constant despite changes in the background noise.

Finally, numerical analysis has shown that the non-uniform sampling strategy yields results, in terms of probability of detection and of false alarm, which are comparable to the ones returned by the more standard $\lambda/2$ sampling, with much fewer data. Indeed, uniform sampling returns better results only for low SNR. This could be expected and it is the trade-off for reducing the number of data. This drawback can be partially remedied by increasing the number of data through a higher oversampling factor ν.

REFERENCES

[1] B.-K. Yeo and Y. Lu, "Array failure correction with a genetic algorithm," *IEEE Trans. Antennas Propag.*, vol. 47, no. 5, pp. 823–828, May 1999.
[2] A. Dell'Aversano, A. Natale, A. Cuccaro, and R. Solimene, "Linear array antenna diagnostics through a MUSIC algorithm," *IEEE Access*, vol. 7, pp. 176952–176959, 2019.
[3] A. Patnaik, B. Chowdhury, P. Pradhan, R. K. Mishra, and C. Christodolou, "An ANN application for fault finding in antenna arrays," *IEEE Trans. Antennas Propag.*, vol. 55, no. 3, pp. 775–777, Mar. 2007.
[4] S. Vigneshwaran, N. Sundararajan, and P. Saratchandran, "Direction of arrival (DOA) estimation under array sensor failures using a minimal resource allocation neural network," *IEEE Trans. Antennas Propag.*, vol. 55, no. 2, pp. 334–343, Feb. 2007.
[5] Y. Rahmat-Samii, "Microwave holographic metrology for antenna diagnosis," *IEEE Antennas Propag. Soc. Newslett.*, vol. 29, no. 3, pp. 5–16, Jun. 1987.
[6] A. Buonanno, M. D'Urso, M. Cicolani, and S. Mosca, "Large phased arrays diagnostic via distributional approach," *Prog. Electromagn. Res.*, vol. 92, pp. 153–166, 2009.
[7] A. Buonanno and M. D'Urso, "A novel strategy for the diagnosis of arbitrary geometries large arrays," *IEEE Trans. Antennas Propag.*, vol. 60, no. 2, pp. 880–885, Feb. 2012.
[8] J. J. Lee, E. M. Ferren, D. P. Woollen, and K. M. Lee, "Near-field probe used as a diagnostic tool to locate defective elements in an array antenna," *IEEE Trans. Antennas Propag.*, vol. AP-36, no. 6, pp. 884–889, Jun. 1988.
[9] O. M. Bucci, M. D. Migliore, G. Panariello, and P. Sgambato, "Accurate diagnosis of conformal arrays from near-field data using the matrix method," *IEEE Trans. Antennas Propag.*, vol. 53, no. 3, pp. 1114–1120, Mar. 2005.
[10] M. A. Maisto, R. Solimene, and R. Pierri, "Valid angle criterion and radiation pattern estimation via singular value decomposition for planar scanning," *IET Microw., Antennas Propag.*, vol. 13, no. 13, pp. 2342–2348, Oct. 2019.
[11] M. D. Migliore, "A compressed sensing approach for array diagnosis from a small set of near-field measurements," *IEEE Trans. Antennas Propag.*, vol. 59, no. 6, pp. 2127–2133, Jun. 2011.
[12] M. D. Migliore, "Array diagnosis from far-field data using the theory of random partial Fourier matrices," *IEEE Antennas Wireless Propag. Lett.*, vol. 12, pp. 745–748, 2013.

[13] C. Xiong, G. Xiao, Y. Hou, and M. Hameed, "A compressed sensing-based element failure diagnosis method for phased array antenna during beam steering," *IEEE Antennas Wireless Propag. Lett.*, vol. 18, no. 9, pp. 1756–1760, Sep. 2019.
[14] Z. Lin, Y. Chen, X. Liu, R. Jiang, and B. Shen, "A Bayesian compressive sensing-based planar array diagnosis approach from near-field measurements," *IEEE Antennas Wireless Propag. Lett.*, vol. 20, no. 2, pp. 249–253, Feb. 2021.
[15] W. Li, W. Deng, and M. D. Migliore, "A deterministic far-field sampling strategy for array diagnosis using sparse recovery," *IEEE Antennas Wireless Propag. Lett.*, vol. 17, no. 7, pp. 1261–1265, Jul. 2018.
[16] D. L. Donoho, "Compressed Sensing," *IEEE Trans. Inf. Theory*, vol. 52, no. 4, pp. 1289–1306, Jan. 2006.
[17] E. J. Candès and M. B. Wakin, "An introduction to compressive sampling," *IEEE Signal Process. Mag.*, vol. 25, no. 2, pp. 21–30, Mar. 2008.
[18] R. Solimene, M. A. Maisto, and R. Pierri, "Sampling approach for singular system computation of a radiation operator," *J. Opt. Soc. Amer. A, Opt. Image Sci.*, vol. 36, no. 3, pp. 353–361, 2019.
[19] M. A. Maisto, R. Solimene, and R. Pierri, "Metric entropy in linear inverse scattering," *Adv. Electromagn.*, vol. 5, no. 2, pp. 46–52, 2016.
[20] M. A. Maisto, R. Pierri, and R. Solimene, "Near-field transverse resolution in planar source reconstructions," *IEEE Trans. Antennas Propag.*, vol. 69, no. 8, pp. 4836–4845, Aug. 2021.
[21] M. Maisto, R. Pierri, and R. Solimene, "Near-field warping sampling scheme for broad-side antenna characterization," *Electronics*, vol. 9, no. 6, p. 1047, Jun. 2020.
[22] M. A. Maisto, G. Leone, A. Brancaccio, and R. Solimene, "Efficient planar near-field measurements for radiation pattern evaluation by a warping strategy," *IEEE Access*, vol. 9, pp. 62255–62265, 2021.
[23] N. Levanon, *Radar Principle*. New York, NY, USA: Wiley, 1988.
[24] M. Bertero, P. Boccacci, and C. De Mol, *Introduction to Inverse Problems in Imaging*, 2nd ed. Boca Raton, FL, USA: CRC Press, 2021.
[25] A. Brancaccio and R. Solimene, "Fault detection in dielectric grid scatterers," *Opt. Exp.*, vol. 23, no. 7, pp. 8200–8215, 2015.

MARIA ANTONIA MAISTO (Member, IEEE) received the M.S. degree *(summa cum laude)* in electronic engineering and the Ph.D. degree in electronic and computer science engineering from the University of Campania, Aversa, Italy, in 2012 and 2015, respectively. Since 2016, she has been a Postdoctoral Fellow with the Department of Engineering, Università della Campania. Her current research interests include electromagnetic inverse problems with particular attention to theoretical and numerical aspects. In particular, they include electromagnetic inverse source and inverse scattering problems, electromagnetic field information content, microwave radar imaging, RCS estimation from near-field measurements, and electromagnetic field sampling.

MARIO DEL PRETE received the M.S. degree *(summa cum laude)* in electronic engineering from the University of Campania, Aversa, Italy, in 2021. He is currently pursuing the Ph.D. degree in industrial and information engineering with the Department of Engineering, Università della Campania "Luigi Vanvitelli." His current research interests include electromagnetic inverse source problems, electromagnetic field sampling, and antenna diagnostics.

GIOVANNI LEONE (Member, IEEE) received the Laurea degree in electronic engineering from the University of Naples Federico II, Naples, Italy, in 1981. From 1986 to 1992, he was an Associate Researcher in electromagnetics with the University of Salerno, Italy. From 1992 to 2000, he was an Associate Professor with the University of Salerno and the Seconda Universitá degli Studi di Napoli, Italy. He is currently a Full Professor with the University of Campania "Luigi Vanvitelli," Italy. He was responsible for research funding from the Italian Space Agency, Rome, Italy, the National Research Council, and the Ministry of Scientific Research. His current research interests include antenna measurement techniques and synthesis, phase retrieval of radiated fields, inverse scattering for non-destructive diagnostics, microwave tomography for subsurface sensing, and conformal antennas diagnostics.

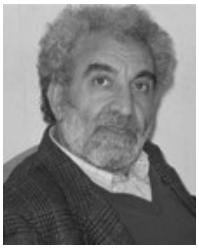

ROCCO PIERRI received the Laurea degree *(summa cum laude)* in electronic engineering from the University of Naples "Federico II," in 1976. He was a Visiting Scholar with the University of Illinois Urbana–Champaign, Urbana, IL, USA; Harvard University, Cambridge, MA, USA; Northeastern University, Boston, MA, USA; Supelec, Paris, France; and the University of Leeds, Leeds, U.K. He also extensively lectured abroad in many universities and research centers. He is currently a Full Professor with the University of Campania "Luigi Vanvitelli," Aversa, Italy. His current research interests include antennas, phase retrieval, near-field techniques, inverse electromagnetic scattering, subsurface sensing, electromagnetic diagnostics, microwave tomography, inverse source problems, and information content of radiated field. He was a recipient of the 1999 Honorable Mention for the H. A. Wheeler Applications Prize Paper Award of the IEEE Antennas and Propagation Society.

RAFFAELE SOLIMENE (Senior Member, IEEE) received the Laurea *(summa cum laude)* and Ph.D. degrees in electronic engineering from the Seconda Universitá degli Studi di Napoli (SUN), Aversa, Italy, in 1999 and 2003, respectively. In 2002, he became an Assistant Professor with the Faculty of Engineering, Mediterranea University of Reggio Calabria, Italy. Since 2006, he has been with the Dipartimento di Ingegneria, University of Campania "Luigi Vanvitelli," where he is currently an Associate Professor. Based on the following topics, he has coauthored more than 250 scientific works. His research interests include inverse electromagnetic problems with applications to inverse source and array diagnostics, non-destructive subsurface investigations, through-the-wall and GPR imaging, and breast cancer detection. On these topics, he routinely serves as a reviewer for a number of journals, organized several scientific sessions and edited a number of special issues. He is also an Associate Editor of four scientific journals, among which IEEE Geoscience and Remote Sensing Letters.